

Mechano-Optical Analysis of Single Cells with Transparent Microcapillary Resonators

*Original*

Mechano-Optical Analysis of Single Cells with Transparent Microcapillary Resonators / MARTIN PEREZ, Alberto.; Ramos, D.; Gil-Santos, E.; Garcia-Lopez, S.; Yubero, M. L.; Kosaka, P. M.; San Paulo, A.; Tamayo, J.; Calleja, M.. - In: ACS SENSORS. - ISSN 2379-3694. - 4:12(2019), pp. 3325-3332. [10.1021/acssensors.9b02038]

*Availability:*

This version is available at: 11583/2985144 since: 2024-01-16T12:08:03Z

*Publisher:*

American Chemical Society

*Published*

DOI:10.1021/acssensors.9b02038

*Terms of use:*

This article is made available under terms and conditions as specified in the corresponding bibliographic description in the repository

*Publisher copyright*

(Article begins on next page)

# Mechano-Optical Analysis of Single Cells with Transparent Microcapillary Resonators

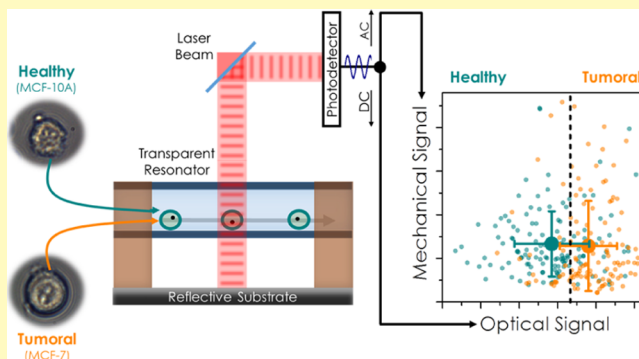
Alberto Martín-Pérez,<sup>1</sup> Daniel Ramos,<sup>2\*</sup> Eduardo Gil-Santos, Sergio García-López, Marina L. Yubero, Priscila M. Kosaka, Alvaro San Paulo,<sup>2</sup> Javier Tamayo, and Montserrat Calleja<sup>2\*</sup>

Bionanomechanics Lab, Instituto de Micro y Nanotecnología, IMN-CNM (CSIC), Isaac Newton 8 (PTM), E-28760 Tres Cantos, Madrid, Spain

## Supporting Information

**ABSTRACT:** The study of biophysical properties of single cells is becoming increasingly relevant in cell biology and pathology. The measurement and tracking of magnitudes such as cell stiffness, morphology, and mass or refractive index have brought otherwise inaccessible knowledge about cell physiology, as well as innovative methods for high-throughput label-free cell classification. In this work, we present hollow resonator devices based on suspended glass microcapillaries for the simultaneous measurement of single-cell buoyant mass and reflectivity with a throughput of 300 cells/minute. In the experimental methodology presented here, both magnitudes are extracted from the devices' response to a single probe, a focused laser beam that enables simultaneous readout of changes in resonance frequency and reflected optical power of the devices as cells flow within them. Through its application to MCF-7 human breast adenocarcinoma cells and MCF-10A nontumorigenic cells, we demonstrate that this mechano-optical technique can successfully discriminate pathological from healthy cells of the same tissue type.

**KEYWORDS:** microcapillary resonators, label-free cell cytometry, cell biophysics, cell phenotyping, hollow microchannel resonators, mass sensors, refractive index sensors, microparticle classification, nanomechanical sensors



The interest for the characterization of single cells in flow started as early as 1934 when Moldavan studied cells flowing in a glass capillary by a photoelectric device.<sup>1</sup> Today, thanks to the use of fluorescent tags, modern flow cytometers can provide tens of measurement parameters simultaneously,<sup>2</sup> and they serve as ideal platforms for the isolation of target cells for single-cell sequencing<sup>3</sup> and a first-choice tool for immunophenotyping of peripheral blood cells in hematological diseases.<sup>4</sup> Although the use of fluorescent reporters is an indisputable success in flow cytometry, avoiding cell labeling has also been a most endeavored route in the field, as fluorescent reporters can alter the cell life cycle and interfere with the biological processes under study. The labeling process itself faces challenges because of the phenotypic heterogeneity of diseased cells, which demands careful design of labeled antibodies to cell-surface antigens to avoid misleading classification of cell types.<sup>5</sup> Label-free cell classification is advantageous because of simplified sample preparation and the capability to run nontargeted tests to find new or undefined cell populations.<sup>6</sup> Moreover, cell biophysical parameters are closely related to cell health status, cell life cycle stage, and cell–cell interactions,<sup>7–12</sup> so new techniques enabling further single cell biophysics research may enable new discoveries.<sup>13–15</sup> The first step to investigate pathological cell phenotypes from complex cell populations is cell sorting. To

this end, label-free techniques usually demand the measurement of several parameters simultaneously and with high throughput<sup>16–18</sup> because of the inherent morphological heterogeneity of same type cells, even those from the same cell line.<sup>19</sup> Imaging flow cytometry has succeeded by combining the optical characterization of cell size and morphology,<sup>9,20,21</sup> refractive index,<sup>11,12</sup> or deformability,<sup>22–24</sup> with proven capability for label-free cell screening in leukemia diagnosis.<sup>25</sup> A more recent route in label-free cytometry proposes the use of mechanical sensors to track cell physical properties.<sup>8,10,26–28</sup> This mechanical route has harnessed mainly the measurement of cell buoyant mass,<sup>29</sup> this technique<sup>8,26</sup> has demonstrated capability to identify cancerous epithelial cells spiked in blood<sup>26</sup> and to follow cell stiffness changes during mitosis.<sup>8</sup>

The choice of the cell biophysical properties to be tracked is critical to achieve a fully functional test because it determines both the classification accuracy of the technique and the type of biological processes made available to research. We propose here the simultaneous measurement of cell mass and optical reflectivity by using doubly clamped transparent capillary

**Received:** October 17, 2019

**Accepted:** November 29, 2019

**Published:** November 29, 2019

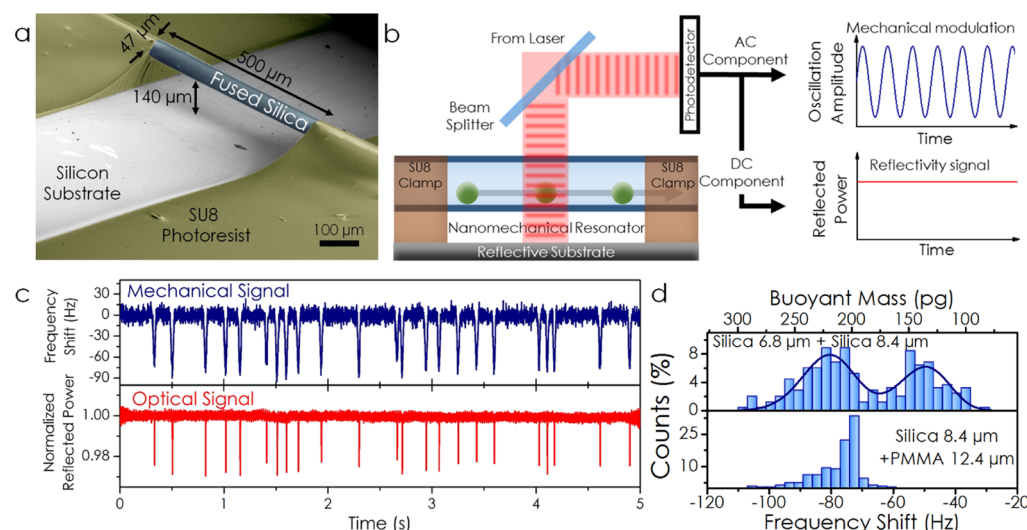


**Figure 1.** Mechano-optical characterization of single particles. (a) Scanning electron microscopy image of a suspended hollow resonator device fabricated from a glass capillary. The polymer pads and the fused silica capillary are depicted in false color. (b) Schematics of the experimental setup. The suspended capillary is illuminated by a laser beam; the reflected signal is directed to a photodiode, and the voltage signal is analyzed by splitting the ac/dc components. The ac component provides the vibration amplitude of the capillary, and the dc component provides the reflected optical power. (c) Upper chart/blue line. Real-time measurement of the frequency shift, acquired through the ac signal. Lower chart/red line. Real-time measurement of the normalized reflected power acquired through the dc signal. The abrupt changes in the optical and mechanical signals are caused by 8.4 μm silica particles flowing through the resonator. (d) Buoyant mass measurement of single particles with capillary resonators. Upper chart: experimental measurement of the frequency shift and resulting buoyant mass for a mixture of 8.4 and 6.8 μm diameter silica particles. Lower chart: experimental measurement of the frequency shift and resulting buoyant mass of a mixture of 12.4 μm diameter PMMA particles and 8.4 μm diameter silica particles. The resulting distribution for this mixture does not present two maxima; it is not possible to classify the particles into each family because of their similar buoyant masses.

mechanical resonators, with the aim of classifying morphologically similar cells while retaining the capability to measure single-cell buoyant mass. The reason to address these two biophysical parameters for cell analysis and sorting is twofold. On the one hand, imaging cytometry and characterization of the cell refractive index have proven high classification accuracy among label-free techniques. On the other hand, cell mechanics demonstrates a high potential to understand and follow relevant processes of cell biology, where cell mass is a particularly relevant biophysical parameter to study. SMRs, suspended microchannel resonators, have demonstrated their use in tracking the effect of drugs on the buoyant mass and mass accumulation rate of cells, and they have proven to possess a prognostic value for such measurements for multiple myeloma.<sup>10</sup> In SMR devices, a carrier liquid containing the analytes flows inside a mechanical resonator, while its resonance frequency is measured in real time to track the buoyant mass of the particles. These devices have been able to merge all advantages of microfluidics for high-throughput analysis with very high mass resolution,<sup>29–33</sup> on the verge of 10 ag for real-time analysis of nanoparticles in physiological environments,<sup>34</sup> and 50 fg buoyant mass resolution for mammalian blood cells.<sup>27,29,35</sup> Despite this high resolution, the buoyant mass parameter alone does not suffice to classify different cells when their buoyant mass is very similar. Cavity optomechanical devices able to track additional mechanical parameters, as particle compressibility, have been proposed to discern between microparticles that do not show density contrast.<sup>36,37</sup> Still, these devices have not yet been applied to cell analysis.

In this work, we demonstrate an experimental methodology based on transparent microcapillary resonator (TMR) devices and interferometric readout for the simultaneous character-

ization of the buoyant mass and optical reflectivity of living cells that flow within them. TMRs presented here are doubly clamped hollow mechanical resonator devices based on fused silica glass microcapillaries<sup>38–44</sup> with a mechanical frequency stability of  $\sim 10^{-7}$  for the first flexural mode, allowing a buoyant mass resolution of 0.6 pg. In this study, we first analyze the performance of our TMR devices to detect and classify inorganic calibration particles of diverse sizes and material properties, and then use them with two cell lines, MCF-7 human breast adenocarcinoma cells and MCF-10A human epithelial breast cells, as a proof of principle of the capability of this mechano-optical technique to discern pathological cells from physiological cells from the same tissue type.

## RESULTS AND DISCUSSION

The TMRs developed in this work consist of hollow cylinders with 47 μm outer diameter and 38 μm inner diameter, obtained by stretching silica capillary tubes and integrating them on a silicon chip by means of polymeric pads placed 500 μm apart, as schematically depicted in Figure 1a (further details about the fabrication process are provided in the Experimental Section). The transparent glass material, which the resonators are made of, provides optical access to the analytes that flow within them. The suspended resonator is actuated by using a piezoelectric transducer and its first flexural mode is optically detected<sup>44</sup> by focusing a laser beam on the middle of the suspended region of the capillary, Figure 1b, obtaining a resonance frequency of 668 kHz. The laser beam intensity is modulated at the mechanical resonance frequency (ac component, Figure 1b); moreover, this same laser serves to optically probe the flowing particles when they pass under the laser beam (dc component, Figure 1b). As described in Figure

1b, the signal coming out from the photodetector is split up into two different components: the dc component, which contains information about the total optical power reflected (optical signal), and the ac component, which is modulated at the mechanical resonance frequency of the resonator (mechanical signal). The device is connected at each end to a microfluidic pump which allows setting a constant and pulseless flow inside the microcapillary. Therefore, by measuring the mechanical resonance frequency as a function of time while flowing a carrier liquid containing the analytes, we can measure the buoyant mass of each single particle passing through the channel. In the upper chart of Figure 1c, we show the real-time tracking of the resonance frequency shift of the fundamental flexural mode of a device filled with ultrapure water containing silica particles of 8.4  $\mu\text{m}$  diameter (blue curve). In this configuration, the Allan deviation reaches a value of  $3 \times 10^{-7}$  for an integration time of 150 ms, which implies a mass resolution of 0.6 pg<sup>44</sup> (further details about the determination of these parameters are provided in the Supporting Information). Each passing particle produces a shift in the mechanical resonance frequency, measured from the ac mechanical signal and represented in blue in the upper chart in Figure 1c. In the lower chart of Figure 1c, we show the normalized reflected power obtained from the dc optical signal (red line). The reflected power drops because of the scattering produced by the flowing particles. Consequently, we acquire simultaneously two signals from each flowing particle, one optical signal and one mechanical signal, arising each from the dc and ac components of the optical readout, respectively.

The first advantage of simultaneously tracking a mechanical and an optical signal is the ability to discern between single analytes and clusters of two or more analytes flowing inside the capillary resonator. We must note that the time span for the mechanical and optical signals is not the same. The laser spot diameter, of about 20  $\mu\text{m}$ , determines the sensing area for the optical signal, as particles are detected optically only when entering this region. For the mechanical signal, although the vibrations are measured at one single point determined by the laser spot, the particles shift the mechanical frequency of the capillary while passing through the full length of its suspended region (500  $\mu\text{m}$ ). According to Rayleigh approximation<sup>45</sup> and neglecting the stiffness term,<sup>46</sup> the frequency shift is proportional to  $\Delta f \propto (m_b \psi_n^2(x_0))^{-1}$ , where  $\psi_n(x_0)$  is the  $n$ th mode profile at the particle position  $x_0$ , see the Experimental Section for further details. Therefore, each particle passing through the resonator probes the mechanical mode from its entering to its outing position between the two clamping points of the resonator. Since the optical signal, measured as the reflected optical power variation, follows the laser Gaussian profile, even particles separated a distance shorter than the laser spot diameter can be resolved. The Supporting Information provides further details about the measurement of the optical and mechanical signals of a single particle, a dimer, and two separate particles traveling closer than the capillary length. In previous works, this problem was either avoided by delaying the entrance of the particles to the resonator<sup>28</sup> or solved by the simultaneous tracking of, at least, four vibration modes.<sup>47</sup>

In order to test the performance of our TMR devices to discern analytes according to their buoyant masses, we have measured the frequency shifts caused by monodisperse particles and particle mixtures in solution. The results for a 1:1 mixture of silica microparticles 8.4 and 6.8  $\mu\text{m}$  in diameter are shown in the upper blue histogram in Figure 1d, where we

can distinguish the two particle populations, obtaining a buoyant mass of  $138 \pm 35$  pg (expected  $132 \pm 23$  pg from the nominal densities) for the 6.8  $\mu\text{m}$  diameter particles and  $222 \pm 30$  pg (expected  $248 \pm 18$  pg) for the 8.4  $\mu\text{m}$  diameter particles. However, when we repeat the same experiment with particles of different materials and size, but similar buoyant masses, the two subpopulations cannot be resolved. The lower blue histogram in Figure 1d shows the measured frequency shifts and corresponding buoyant masses for a mixture of silica particles 8.4  $\mu\text{m}$  in diameter and poly(methyl methacrylate) PMMA 12.4  $\mu\text{m}$  diameter particles. Even though the size of PMMA and silica particles is very different, the two particle populations are indistinguishable through the resonance frequency shift measurements alone. When repeating these measurements sequentially for dilutions of only one type of particle, we obtain a very similar buoyant mass,  $m_b^{\text{PMMA}} = 199 \pm 9$  pg (expected  $180 \pm 9$  pg) and  $m_b^{\text{silica}, 8.4 \mu\text{m}} = 220 \pm 15$  pg, (expected  $248 \pm 18$  pg). The Experimental Section and Supporting Information contain full data of the SEM characterization of the size distribution for the different particle populations used.

In order to show the additional optical reflectivity signal provides the means to discern analyte populations of similar buoyant masses, we have compared the normalized reflectivity signals from monodisperse solutions of silica particles 8.4  $\mu\text{m}$  in diameter and PMMA particles 12.4  $\mu\text{m}$  in diameter. Figure 2a shows real-time tracking of the normalized reflected power

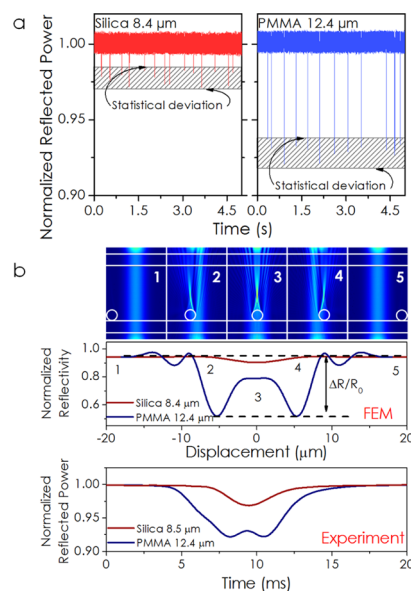


**Figure 2.** Optical characterization of particles flowing through the capillary resonator. (a) Real-time measurements of the normalized reflected power for 8.4  $\mu\text{m}$  diameter silica (red curve) and 12.4  $\mu\text{m}$  diameter PMMA (blue curve) particles. The reflectivity change is in order of magnitude larger for the PMMA particles due both to their larger size and refractive index. (b) Upper chart: finite element simulations of the norm of the electric field for different positions of a particle passing through a suspended capillary filled with water and illuminated by a 20  $\mu\text{m}$  diameter laser beam. Mid chart: normalized reflectivity of simulated 8.4  $\mu\text{m}$  diameter silica and 12.4  $\mu\text{m}$  diameter PMMA particles flowing in water through the capillary. Lower chart: experimental measurements of the normalized reflected power of a 12.4  $\mu\text{m}$  diameter PMMA particle and an 8.4  $\mu\text{m}$  diameter silica particle flowing in ultrapure water through the capillary device shown in Figure 1.



from these two particle solutions. The normalized reflectivity signal shows four times larger reflectivity change for the PMMA particles than for the silica particles. We attribute this to the differences in size and refractive index of the two particle types. Thus, to further understand the optical signals acquired for the flowing particles in our setup, we have performed finite element simulations of the electric field norm distribution (Figure 2b). In these simulations, we have reproduced the geometry of the capillary tube and experimental particle position. We have confirmed through the CCD images that in our experimental configuration, all particles travel close to the tube wall; this is due to the hydrodynamic forces exerted by the fluid. The capillary devices are suspended over a silicon substrate that acts as a mirror, forming a Fabry–Perot cavity underneath; actually, the whole system can be viewed as a multilayer cavity. The plots in Figure 2b represent a 2D transversal slice of the capillary illuminated from the top (see the Supporting Information for further details about the finite element simulations). The laser light travels through different media: air/fused silica/water/particle/fused silica/air/bulk silicon. We collect the total reflected power from the upper boundary and identify five different positions of the silica or PMMA particle with respect to the laser beam: before and after particle–light interaction (positions labeled as 1 and 5 in Figure 2b), two symmetrical positions where the scattered light is most deviated from the normal incidence direction (positions labeled as 2 and 4), and the central position, where the light travels through the full particle diameter (position 3). All of these features appear in the simulated normalized reflectivity plot of Figure 2b, where we have included the numeric labels indicating the position of the particle respect to the laser beam. The lower chart of Figure 2b shows the experimental normalized reflected power when an 8.4  $\mu\text{m}$  diameter silica particle (dark red curve) and a PMMA 12.4  $\mu\text{m}$  diameter particle (dark blue curve) travel through the laser beam. The experimental profiles and the simulations are qualitatively very similar. Remarkably, for the silica particle, the two symmetrical minima in the scattered light are not observed because the ratio of the laser beam waist/particle diameter is larger than 1; thus, for smaller particles than those used here, the signal to noise ratio might be too low for particle tracking. Still, the readout of the optical signal could be optimized for smaller particles than those used in this work by simply reducing the laser spot diameter. In consideration of these results, the optical signature we will use from now on to identify different particles is defined as  $\Delta R/R_0$ , where  $\Delta R = R_p - R_0$ ;  $R_p$  is the reflected power minima, when the particle is under the laser beam (positions 2 and 4), and  $R_0$  is the reflected power when no particle interacts with the laser beam (positions 1 and 5). We have calibrated the devices with liquids of a well-known refractive index and found that this configuration translates into a sensitivity to the refractive index of  $10^{-5}$ ; see the Supporting Information for calibration curves.

In Figure 3, we show the acquired optical and mechanical signals for silica particles (gray symbols for 6.8  $\mu\text{m}$  diameter and red symbols for 8.4  $\mu\text{m}$  diameter particles), polystyrene (PS) particles (magenta symbols for 10  $\mu\text{m}$  and green symbols for 19  $\mu\text{m}$  diameter), and 12.4  $\mu\text{m}$  PMMA particles (blue symbols). We have represented the mechanical signal in the y-axis and the optical signal in the x-axis in a 2D scatter plot, where we can clearly separate the five microparticle populations. The measurements shown as a 2D scatter plot are also presented as histograms for the buoyant mass obtained

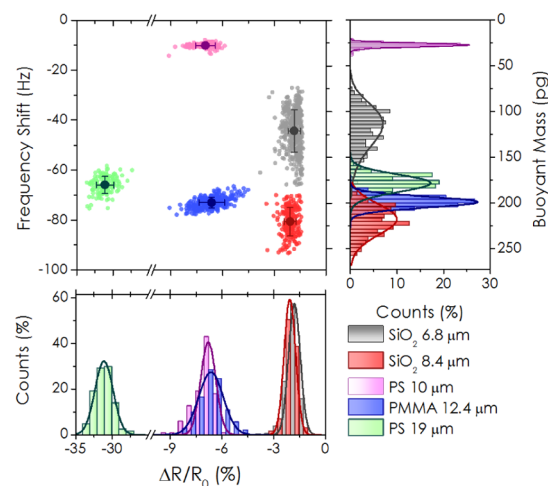


**Figure 3.** Mechano-optical characterization of microparticles. The 2D scatter plot of the experimental frequency shift and reflectivity signals for silica ( $\text{SiO}_2$ ) particles (6.8  $\mu\text{m}$ , gray symbols,  $N = 432$ , and 8.4  $\mu\text{m}$ , red symbols,  $N = 205$ ), PS particles (10  $\mu\text{m}$ , magenta symbols,  $N = 152$ , and 19  $\mu\text{m}$ , green symbols,  $N = 131$ ), and PMMA 12.4  $\mu\text{m}$  particles (blue symbols,  $N = 311$ ). The dilutions of each type of particle have been flown sequentially through the microcapillary resonator. The projection in y-axis depicts the buoyant mass extracted from the frequency shifts for the measured particles. The projection in the x-axis shows the reflectivity change,  $\Delta R/R_0$ , for the particles flowing under the laser beam. Silica particles differing in 1.8  $\mu\text{m}$  in diameter cannot be distinguished by using the optical signal alone, as well as PS and PMMA particles; while 8.4  $\mu\text{m}$   $\text{SiO}_2$ , 12.4  $\mu\text{m}$  PMMA, and 19  $\mu\text{m}$   $\text{SiO}_2$  silica particles cannot be classified by characterizing their buoyant mass alone. The combination of the two parameters allows a clear discrimination of the five populations of particles. For a better understanding, dimers have been removed in this plot; see the Supporting Information for further details about dimers.

from the measured frequency shifts (y-axis) and for the reflectivity change (x-axis). The results show that there are two pairs of populations that cannot be distinguished by the optical method alone (both silica particles, PMMA, and PS 10  $\mu\text{m}$  particles). In the case of silica particles, the similar reflectivity distribution is because of their similar size compared to the laser spot and their identical material properties; while in the case of PMMA and PS 10  $\mu\text{m}$  particles, the similar reflectivity change is because of the uncertainty arising from the sinusoidal dependence of the reflectivity with the refractive index in the interferometric detection (see S4 in the Supporting Information for further details). On the other hand, there are two pairs of particles indistinguishable from the buoyant mass measurements alone: PS 19  $\mu\text{m}$  and PMMA particles, with measured buoyant masses of  $m^{\text{PS}19} = 180 \pm 9$  pg and  $m^{\text{PMMA}} = 199 \pm 9$  pg (expected  $180 \pm 14$  and  $180 \pm 9$  pg) and silica 8.4  $\mu\text{m}$  particles  $m_b^{\text{silica},8.4\mu\text{m}} = 220 \pm 15$  pg (expected  $248 \pm 18$  pg). The combined measurements of both mechanical and optical signals in the 2D scatter plot produce well-separated clusters of points with no overlap among them, allowing unequivocal classification of the microparticles into the five different populations.

We have applied the methodology described above to the analysis of cells from two distinct cell lines of the same tissue type, MCF-10A, a cell line representative of nontumorigenic human breast epithelial cells, and MCF-7, a tumorigenic cell line. The diameters of these cells are  $17 \pm 2$   $\mu\text{m}$  (MCF-10A) and  $19 \pm 3$   $\mu\text{m}$  (MCF-7) according to the optical microscopy

measurements performed (further details provided in the Supporting Information). Figure 4a,b shows representative

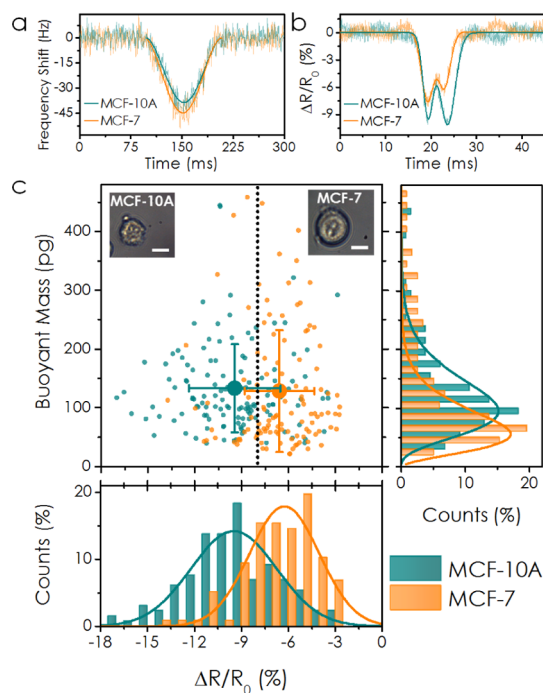


**Figure 4.** Mechano-optical characterization of healthy and pathological cells. (a) Representative measurement of the frequency shift for a single MCF-10A cell (green line) and a single MCF-7 cell (orange line) flowing inside the capillary resonator. (b) Representative measurement of the normalized reflected power for a single MCF-10A cell (green line) and a single MCF-7 cell (orange line) flowing inside the capillary resonator. The insets show optical images of MCF-10A and MCF-7 cells, both suspended in PBS with 5% DMSO. (c) 2D scatter plot of the experimental frequency shifts and reflectivity signals acquired for dilutions of MCF-10A ( $N = 131$ ) and MCF-7 cells ( $N = 117$ ), both suspended in PBS buffer with a 5% of DMSO flowing through the capillary resonator. The projection in y-axis depicts the buoyant mass extracted from the frequency shifts for the measured cells. The projection in the x-axis shows the reflectivity change,  $\Delta R/R_0$ , for the flowing cells. Cells from both cell lines cannot be classified through the measurement of the buoyant mass alone, but the optical characterization allows separating the pathological and healthy cells in two distributions with 76% classification accuracy, according to the criteria marked as a dotted line in the 2D plot.

examples of simultaneous frequency shift and normalized reflectivity measurements when a single MCF-10A cell (green line) and a single MCF-7 cell (orange line) flow through a transparent capillary resonator. The registered signals are qualitatively similar to those observed for the inorganic microparticles considered above, which justifies the application of the same methodology for the analysis of the results.

In Figure 4c, we present the mechanical and optical measurements performed in 131 cells of the MCF-10A type (green symbols) and 117 cells of the MCF-7 type (orange symbols). We have used phosphate-buffered saline (PBS) buffer as the carrier liquid in these experiments, with  $n_{\text{PBS}} = 1.335 \pm 0.001$ . The results are presented as a 2D scatter plot with the corresponding histogram projections for each parameter. From the buoyant mass measurements, we obtained average values of  $133 \pm 75$  pg for MCF-10A and  $128 \pm 100$  pg for MCF-7. These values are consistent with the theoretical

values expected from the measured diameters and dispersion in cell size, as well as a typical cell density of  $1.05 \text{ g/mL}$ ,<sup>48</sup> which are  $129 \pm 45$  pg for MCF-10A and  $180 \pm 85$  pg for MCF-7. The measured buoyant mass distributions show a strong overlap between the two cell types, which would make cell classification according to buoyant mass largely impractical in this case.

The reflectivity measurements,  $\Delta R/R_0$ , result in average values of  $-10.5 \pm 2.5\%$  for the MCF-10A type and  $-6.0 \pm 2.0\%$  for the MCF-7 type. The distribution of values of  $\Delta R/R_0$  follows well-defined Gaussian profiles in the x-axis histogram projection for both cell types with some overlap. In order to quantify the classification accuracy and sensitivity of the assay, we have applied ROC analysis, the classification accuracy being defined as the ratio of true to total results for a given classification criterion and the sensitivity (or true positive rate) as the ratio of true positives to the total positives. For the reflectivity distributions of Figure 4c, choosing  $\Delta R/R_0 > -8\%$  (dotted line in Figure 4c) as the classification criterion to define a positive test for the presence of pathological cells results in a classification accuracy of 76% and a sensitivity of 80%. These values support the validity of our approximation, although further technological developments can be expected to optimize the classification performance of the presented mechano-optical approach. To that end, it is worth noting that the reflectivity signal is dominated by two parameters: the cell refractive index and its size. In our case, the measured cells have similar size distributions; thus, we can attribute the reflectivity differences mainly to cell refractive index variations. Tumorigenic cells are expected to show a small increase in their refractive index, related to changes in their architecture, metabolism, and biochemical composition,<sup>49</sup> being the cell refractive index approximately proportional to the cell protein content.<sup>11</sup> Thus, this parameter is expected to increase for the tumorigenic cells due to their enlarged nucleus related to faster cell division. Typical values of the cell refractive index are  $n_{\text{cell}} = 1.36 \pm 0.01$ ,<sup>11</sup> with an expected difference in the refractive index from tumorigenic to healthy cells in the order of  $10^{-2}$ ,<sup>50</sup> well above our estimation of the detection limit of  $10^{-5}$ . Further improvements are expected by optimizing the laser spot diameter, capillary wall thickness, refractive index of the carrier liquid, and length of the optical cavity formed by the capillary and the underlying substrate.

## CONCLUSIONS

We have presented the performance of TMRs for the simultaneous measurement of the buoyant mass and reflectivity of microparticles and cells flowing inside them. In addition to the high mass sensitivity provided by resonance frequency shift measurements, the presented interferometric readout provides high sensitivity to changes in the refractive index of the analytes, which translates into the capability to discriminate between neutrally buoyant particles by optical reflectivity analysis. As a proof of principle, we have been able to classify pathological and physiological cells of the same tissue type with 76% accuracy, while measuring single cell buoyant mass at the same time. We envision the applicability of this technology for label-free cell phenotyping based on cell biophysics. The upstream biophysical characterization of cells has been highlighted as a very useful tool prior to single-cell sequencing,<sup>51</sup> while the tracking of the cell mass accumulation rate has proven to have prognostic value.<sup>10</sup> The devices presented here enable a unique route for the combination of

both types of analysis by the simultaneous access to mechanical and optical cell properties. Aside from the potential of the technique for label-free cell analysis, the transparent devices are compatible with the use of additional lasers and fluorescent tags. This strategy would join biochemical and biophysical methods, enabling the study of cell signaling pathways at the molecular level,<sup>52,53</sup> together their effect on cell biophysics. The simultaneous study of tens of different key proteins from single cells, provided by cell cytometry, together with the single cell biophysical analysis provided by mass and reflectivity analysis shown here, could largely contribute to increase our understanding of how cell biochemistry and biophysics are related and serve for innovative diagnostic and drug efficacy tests.

## ■ EXPERIMENTAL SECTION

**Resonance Frequency Measurements.** As a particle flows through the suspended area, it produces a frequency shift proportional to  $\Delta f \propto (m_b \psi_n^2(x_0))^{-1}$ , where  $\psi_n(x_0)$  is the  $n$ th mode profile at the particle position,  $x_0$ , and is given by  $\psi_n(x) = \cos\left(\frac{x\beta_n}{L}\right) - \cosh\left(\frac{x\beta_n}{L}\right) + \frac{\cos\beta_n - \cosh\beta_n}{\sin\beta_n - \sinh\beta_n}$ , and the first eigenval-

$$\left( \sinh\left(\frac{x\beta_n}{L}\right) - \sin\left(\frac{x\beta_n}{L}\right) \right)$$

ues are  $\beta_n = 4.7300, 7.8532, 10.9956, 14.1372, \dots$  For the data analysis dips in the frequency signal produced by flowing particles/cells were fitted to the shape of the first flexural mode by assuming that particles maintain a constant velocity while passing through the suspended region. These fits not only let us obtain the frequency shift but also give the transit time for each particle, which allows calculating directly the velocity of the particle. Frequency shift data obtained by these fittings are converted into buoyant mass by  $\frac{m_b}{m_0} = \left(1 - \frac{f_0}{f_0 + \Delta f}\right) \psi_1(L/2)$ .  $m_0$  is the mass of the resonator (see the

Supporting Information for more details about this parameter), and  $f_0$  is the frequency of the resonator. To characterize the noise level of our readout system, we have calculated the Allan deviation,  $\sigma_{\text{Allan}}(\tau) = \sqrt{\sigma_{\text{Allan}}^2(\tau)}$ , where  $\sigma_{\text{Allan}}^2(\tau)$  is defined as the Allan variance and it is calculated from the average of frequency samples measured in a temporal integration time  $\tau$ ,  $\sigma_{\text{Allan}}^2(\tau) = \frac{1}{2}(\bar{f}(t+1) - \bar{f}(t))^2$ .

**Optical Reflectivity Measurements.** The dc voltage measured by the photodetector (directly proportional to the power light collected) is normalized, with 1 being the power measured when the capillary is filled with the fluid (without a particle), obtaining the normalized reflected power signal. Dips produced in this signal by a particle passing under the spot of the laser are fitted to the sum of two Gaussians. The reflectivity change ( $\Delta R$ ) is obtained from the minimum of this function. In the case of cells and big particles, in which there are two minima, the value of  $\Delta R$  is obtained by averaging both minima.

**Acquisition Rate.** Given the time-scale difference between both signals, the mechanical signal (ac component) was acquired with a 1.7 kHz acquisition rate, while the optical signal was acquired at 13 kHz.

**Buoyant Mass.** The concept of buoyant mass comes out from the Archimedes' principle: an object immersed in liquid experiences a force equal to the weight of the displaced fluid. Thus, the buoyant mass of a spherical particle is defined as  $m_b = \frac{4\pi}{3}\Delta\rho r^3$ , where  $\Delta\rho$  is the difference between the mass density of the particle and fluid and  $r$  is the particle radius. Hence, attending to the particle material and dimensions, it is possible to have particles of different materials and dimensions with the same buoyant mass. For example, a 12.4  $\mu\text{m}$  PMMA particle ( $\rho_{\text{PMMA}} = 1.18 \text{ g/cm}^3$ ) and a 19  $\mu\text{m}$  PS particle ( $\rho_{\text{PS}} = 1.05 \text{ g/cm}^3$ ) in water ( $\rho_{\text{water}} = 1 \text{ g/cm}^3$ ) both present a buoyant mass of 180 pg. The problem of the buoyant mass becomes even more dramatic in the case of disperse particle populations given that two

populations of different particles may be mechanically indiscernible despite having a different average buoyant mass in case both distributions overlap, as shown in Figure 1d. Taking this into account, each particle population presents a Gaussian distribution in its diameter (see the Supporting Information for the morphological characterization of the particles); the buoyant mass distribution will present the following distribution

$$\varphi(m_b) = AB(m_b)^{-3/2} e^{-(B(\sqrt[3]{m_b} - \sqrt[3]{m_{b0}})/\sigma)^2}$$

where  $A$  is an integration constant,  $B$  is a constant given by  $B = \sqrt[3]{6/(\pi\Delta\rho)}$ ,  $m_{b0}$  is the buoyant mass of an average-sized particle, and  $\sigma$  is the diameter of standard deviation.

**Experiments with Microparticles.** For these experiments, spherical silica 6.8  $\mu\text{m}$ , silica 8.4  $\mu\text{m}$ , PMMA 12.4  $\mu\text{m}$  microparticles suspended in aqueous solution (Microparticles GmbH, Ref#SiO<sub>2</sub>-R-6.5, Ref#SiO<sub>2</sub>-R-8.5, Ref#PMMA-R-12.4), PS 10  $\mu\text{m}$ , and PS 19  $\mu\text{m}$  (Microbeads AS, Ref#PS-700, Ref#PS-701) were used. The microparticle suspensions were diluted using ultrapure water to reach concentrations of the order of  $10^6 \text{ mL}^{-1}$  for both silica microparticles,  $10^5 \text{ mL}^{-1}$  for PMMA and PS 10  $\mu\text{m}$  particles, and  $10^4 \text{ mL}^{-1}$  for the PS 19  $\mu\text{m}$  microparticles. Please note that the concentration was decreased as the radii increased to avoid clogging of the resonator.

**Microfluidic Conditions.** Either in the experiments with microparticles or the experiments with cells, the pressure difference given by the microfluidic pump between both ends of the microfluidic circuit was matched to obtain particle velocities in a range from 1 to 10 mm/s. Despite the experimental setup allows us to measure particles with velocities up to 50 mm/s, the upper velocity limit was set to 10 mm/s taking into account that previous works reported that in this type of sensors, buoyant mass can be underestimated if the velocity is high (>10 mm/s) because of pressure effects.<sup>43</sup>

**Cell Culture.** MCF-7 and MCF-10A cell lines were purchased from the American Type Culture Collection (ATCC, USA). MCF-7 cells were grown in Dulbecco's modified Eagle's medium (DMEM, Gibco, Life Technologies Corporation, Rockville, MD, USA) supplemented with 10% FBS, 500 U/mL penicillin, and 0.1 mg/mL streptomycin. MCF-10A cells were cultured in HAM-F12 medium (Gibco) supplemented with 5% horse serum, 20 ng/mL epidermal growth factor, 0.5  $\mu\text{g/mL}$  hydrocortisone, 100 ng/mL cholera toxin, 10  $\mu\text{g/mL}$  insulin, 500 U/mL penicillin, and 0.1 mg/mL streptomycin. All cell lines were maintained at 37 °C in 5% CO<sub>2</sub> in a humidified incubator. For measurements, cells were trypsinized and resuspended, each cell type in its corresponding culture medium (DMEM and HAM-F12). After soft centrifugation, cells were resuspended in a volume of PBS with a 5% of dimethyl sulfoxide (DMSO) such that we obtain a final concentration of  $10^6$  cells/mL. Cells were immediately flown through the capillary resonators after resuspension. We added DMSO to PBS to avoid cell agglomeration and subsequent cell sedimentation in the microcapillary resonator.

## ■ ASSOCIATED CONTENT

### Supporting Information

The Supporting Information is available free of charge at <https://pubs.acs.org/doi/10.1021/acssensors.9b02038>.

Details about the fabrication of the sensors, measurement setup, calibration experiments, and simulations (PDF)

## ■ AUTHOR INFORMATION

### Corresponding Authors

\*E-mail: [daniel.ramos@csic.es](mailto:daniel.ramos@csic.es), (D.R.).

\*E-mail: [montserrat.calleja@csic.es](mailto:montserrat.calleja@csic.es) (M.C.).

### ORCID

Alberto Martín-Pérez: 0000-0001-8233-0764

Daniel Ramos: 0000-0003-2677-4058

Alvaro San Paulo: 0000-0001-9325-8892



Montserrat Calleja: 0000-0003-2414-5725

## Funding

This work was supported by the European Union's Horizon 2020 research and innovation program under European Research Council Grant 681275-LIQUIDMASS-ERC-CoG-2015 and by the Spanish Science, Innovation and Universities Ministry through project CELLTANGLE reference RTI2018-099369-B-I00, project MOMP's reference TEC2017-89765-R and Ramón y Cajal grant RYC-2017-21640 to P.M.K.; by the Comunidad de Madrid (iLUNG B2017/BMD-3884) with support from EU (FEDER, FSE). E.G.-S. received funding from Fundación General CSIC (Programa ComFuturo), as well as Marie-Sklodowska Curie Actions (H2020-MSCA-IF-2015) under NOMBIS project (703354). The service from the Micro and Nanofabrication Laboratory (MiNa) and X-SEM Laboratory, is funded by MCIU (CSIC13-4E-1794) and EU (FEDER, FSE). We have received support for part of the publication fee by CSIC open access publication support initiative through URICI.

## Notes

The authors declare the following competing financial interest(s): Some of the authors are inventors of a related registered patent belonging to their host institution, Agencia Estatal Consejo Superior de Investigaciones Científicas (CSIC).

## ACKNOWLEDGMENTS

We acknowledge the service from the Micro and Nanofabrication Laboratory (MiNa) and X-SEM laboratory at IMN-CSIC.

## REFERENCES

- (1) Moldavan, A. PHOTO-ELECTRIC TECHNIQUE FOR THE COUNTING OF MICROSCOPICAL CELLS. *Science* **1934**, *80*, 188–189.
- (2) Peretto, S. P.; Chattopadhyay, P. K.; Roederer, M. Seventeen-colour flow cytometry: unravelling the immune system. *Nat. Rev. Immunol.* **2004**, *4*, 648–655.
- (3) Saliba, A.-E.; Westermann, A. J.; Gorski, S. A.; Vogel, J. Single-cell RNA-seq: advances and future challenges. *Nucleic Acids Res.* **2014**, *42*, 8845–8860.
- (4) Brown, M.; Wittwer, C. Flow Cytometry: Principles and Clinical Applications in Hematology. *Clinical Chemistry* **2000**, *46*, 1221–1228.
- (5) Wang, L.; Balasubramanian, P.; Chen, A. P.; Kummur, S.; Evrard, Y. A.; Kinders, R. J. Promise and limits of the CellSearch platform for evaluating pharmacodynamics in circulating tumor cells. *Semin. Oncol.* **2016**, *43*, 464–475.
- (6) Carey, T. R.; Cotner, K. L.; Li, B.; Sohn, L. L. Developments in label-free microfluidic methods for single-cell analysis and sorting. *Wiley Interdiscip. Rev.: Nanomed. Nanobiotechnol.* **2019**, *11*, e1529–e1545.
- (7) Chang, Y.-N.; Liang, Y.; Gu, W.; Wang, J.; Qin, Y.; Chen, K.; Li, J.; Bai, X.; Zhang, J.; Xing, G. Microfluidic Analysis for Separating and Measuring the Deformability of Cancer Cell Subpopulations. *ACS Omega* **2019**, *4*, 8318–8323.
- (8) Kang, J. H.; Miettinen, T. P.; Chen, L.; Olcum, S.; Katsikis, G.; Doyle, P. S.; Manalis, S. R. Noninvasive monitoring of single-cell mechanics by acoustic scattering. *Nat. Methods* **2019**, *16*, 263–269.
- (9) Blasi, T.; Hennig, H.; Summers, H. D.; Theis, F. J.; Cerveira, J.; Patterson, J. O.; Davies, D.; Filby, A.; Carpenter, A. E.; Rees, P. Label-free cell cycle analysis for high-throughput imaging flow cytometry. *Nat. Commun.* **2016**, *7*, 10256.
- (10) Cetin, A. E.; Stevens, M. M.; Calistri, N. L.; Fulciniti, M.; Olcum, S.; Kimmerling, R. J.; Munshi, N. C.; Manalis, S. R. Determining therapeutic susceptibility in multiple myeloma by single-cell mass accumulation. *Nat. Commun.* **2017**, *8*, 1613.
- (11) Liu, P. Y.; Chin, L. K.; Ser, W.; Chen, H. F.; Hsieh, C.-M.; Lee, C.-H.; Sung, K.-B.; Ayi, T. C.; Yap, P. H.; Liedberg, B.; Wang, K.; Bourouina, T.; Leprince-Wang, Y. Cell refractive index for cell biology and disease diagnosis: past, present and future. *Lab Chip* **2016**, *16*, 634–644.
- (12) Leblanc-Hotte, A.; Sen Nkwe, N.; Chabot-Roy, G.; Affar, E. B.; Lesage, S.; Delisle, J.-S.; Peter, Y.-A. On-chip refractive index cytometry for whole-cell deformability discrimination. *Lab Chip* **2019**, *19*, 464–474.
- (13) Suresh, S. Biomechanics and biophysics of cancer cells. *Acta Biomater.* **2007**, *3*, 413–438.
- (14) Calzado-Martin, A.; Encinar, M.; Tamayo, J.; Calleja, M.; San Paulo, A. Effect of Actin Organization on the Stiffness of Living Breast Cancer Cells Revealed by Peak-Force Modulation Atomic Force Microscopy. *ACS Nano* **2016**, *10*, 3365–3374.
- (15) Kosaka, P. M.; Calleja, M.; Tamayo, J. Optomechanical devices for deep plasma cancer proteomics. *Semin. Cancer Biol.* **2018**, *52*, 26–38.
- (16) Zheng, Y.; Nguyen, J.; Wei, Y.; Sun, Y. Recent advances in microfluidic techniques for single-cell biophysical characterization. *Lab Chip* **2013**, *13*, 2464–2483.
- (17) Chen, C. L.; Mahjoubfar, A.; Tai, L.-C.; Blaby, I. K.; Huang, A.; Niazi, K. R.; Jalali, B. Deep Learning in Label-free Cell Classification. *Sci. Rep.* **2016**, *6*, 21471.
- (18) Doan, M.; Vorobjev, I.; Rees, P.; Filby, A.; Wolkenhauer, O.; Goldfeld, A. E.; Lieberman, J.; Barteneva, N.; Carpenter, A. E.; Hennig, H. Diagnostic Potential of Imaging Flow Cytometry. *Trends Biotechnol.* **2018**, *36*, 649–652.
- (19) Stockholm, D.; Benchaouir, R.; Picot, J.; Rameau, P.; Neildez, T. M. A.; Landini, G.; Laplace-Builhé, C.; Paldi, A. The Origin of Phenotypic Heterogeneity in a Clonal Cell Population In Vitro. *PLoS One* **2007**, *2*, e394–e406.
- (20) Stavrakis, S.; Holzner, G.; Choo, J.; deMello, A. High-throughput microfluidic imaging flow cytometry. *Curr. Opin. Biotechnol.* **2019**, *55*, 36–43.
- (21) Han, Y.; Gu, Y.; Zhang, A. C.; Lo, Y.-H. Review: imaging technologies for flow cytometry. *Lab Chip* **2016**, *16*, 4639–4647.
- (22) Toepfner, N.; Herold, C.; Otto, O.; Rosendahl, P.; Jacobi, A.; Kräter, M.; Stächele, J.; Menschner, L.; Herbig, M.; Ciuffreda, L.; Ranford-Cartwright, L.; Grzybek, M.; Coskun, Ü.; Reithuber, E.; Garriss, G.; Mellroth, P.; Henriques-Normark, B.; Tregay, N.; Suttorp, M.; Bornhäuser, M.; Chilvers, E. R.; Berner, R.; Guck, J. Detection of human disease conditions by single-cell morpho-rheological phenotyping of blood. *eLife* **2018**, *7*, e29213–e29234.
- (23) Rosendahl, P.; Plak, K.; Jacobi, A.; Kraeter, M.; Toepfner, N.; Otto, O.; Herold, C.; Winzi, M.; Herbig, M.; Ge, Y.; Girardo, S.; Wagner, K.; Baum, B.; Guck, J. Real-time fluorescence and deformability cytometry. *Nat. Methods* **2018**, *15*, 355–358.
- (24) Masaeli, M.; Gupta, D.; O'Byrne, S.; Tse, H. T. K.; Gossett, D. R.; Tseng, P.; Utada, A. S.; Jung, H.-J.; Young, S.; Clark, A. T.; Di Carlo, D. Multiparameter mechanical and morphometric screening of cells. *Sci. Rep.* **2016**, *6*, 37863.
- (25) Dannhauser, D.; Rossi, D.; Ripaldi, M.; Netti, P. A.; Causa, F. Single-cell screening of multiple biophysical properties in leukemia diagnosis from peripheral blood by pure light scattering. *Sci. Rep.* **2017**, *7*, 12666–12678.
- (26) Byun, S.; Son, S.; Amodei, D.; Cermak, N.; Shaw, J.; Kang, J. H.; Hecht, V. C.; Winslow, M. M.; Jacks, T.; Mallick, P.; Manalis, S. R. Characterizing deformability and surface friction of cancer cells. *Proc. Natl. Acad. Sci. U.S.A.* **2013**, *110*, 7580–7585.
- (27) Grover, W. H.; Bryan, A. K.; Diez-Silva, M.; Suresh, S.; Higgins, J. M.; Manalis, S. R. Measuring single-cell density. *Proc. Natl. Acad. Sci. U.S.A.* **2011**, *108*, 10992–10996.
- (28) Calistri, N. L.; Kimmerling, R. J.; Malinowski, S. W.; Touat, M.; Stevens, M. M.; Olcum, S.; Ligon, K. L.; Manalis, S. R. Microfluidic active loading of single cells enables analysis of complex clinical specimens. *Nat. Commun.* **2018**, *9*, 4784.
- (29) Burg, T. P.; Godin, M.; Knudsen, S. M.; Shen, W.; Carlson, G.; Foster, J. S.; Babcock, K.; Manalis, S. R. Weighing of biomolecules,



single cells and single nanoparticles in fluid. *Nature* **2007**, *446*, 1066–1069.

(30) Agache, V.; Blanco-Gomez, G.; Baleras, F.; Caillat, P. An embedded microchannel in a MEMS plate resonator for ultrasensitive mass sensing in liquid. *Lab Chip* **2011**, *11*, 2598–2603.

(31) De Pastina, A.; Maillard, D.; Villanueva, L. G. Fabrication of suspended microchannel resonators with integrated piezoelectric transduction. *Microelectron. Eng.* **2018**, *192*, 83–87.

(32) Calmo, R.; Lovera, A.; Stassi, S.; Chiadò, A.; Scaiola, D.; Bosco, F.; Ricciardi, C. Monolithic glass suspended microchannel resonators for enhanced mass sensing of liquids. *Sens. Actuators, B* **2019**, *283*, 298–303.

(33) Stockslager, M. A.; Olcum, S.; Knudsen, S. M.; Kimmerling, R. J.; Cermak, N.; Payer, K. R.; Agache, V.; Manalis, S. R. Rapid and high-precision sizing of single particles using parallel suspended microchannel resonator arrays and deconvolution. *Rev. Sci. Instrum.* **2019**, *90*, 085004–085013.

(34) Lee, J.; Shen, W.; Payer, K.; Burg, T. P.; Manalis, S. R. Toward Attogram Mass Measurements in Solution with Suspended Nanochannel Resonators. *Nano Lett.* **2010**, *10*, 2537–2542.

(35) Son, S.; Tzur, A.; Weng, Y.; Jorgensen, P.; Kim, J.; Kirschner, M. W.; Manalis, S. R. Direct observation of mammalian cell growth and size regulation. *Nat. Methods* **2012**, *9*, 910–912.

(36) Han, K.; Suh, J.; Bahl, G. Optomechanical non-contact measurement of microparticle compressibility in liquids. *Opt. Express* **2018**, *26*, 31908–31916.

(37) Suh, J.; Han, K.; Peterson, C. W.; Bahl, G. Invited Article: Real-time sensing of flowing nanoparticles with electro-opto-mechanics. *APL Photonics* **2016**, *2*, 010801.

(38) Malvar, O.; Ramos, D.; Martínez, C.; Kosaka, P.; Tamayo, J.; Calleja, M. Highly Sensitive Measurement of Liquid Density in Air Using Suspended Microcapillary Resonators. *Sensors* **2015**, *15*, 7650.

(39) Lee, D.; Kim, J.; Cho, N.-J.; Kang, T.; Kauh, S.; Lee, J. Pulled microcapillary tube resonators with electrical readout for mass sensing applications. *Sci. Rep.* **2016**, *6*, 33799.

(40) Chaudhari, S.; Chaudhari, K.; Kim, S.; Khan, F.; Lee, J.; Thundat, T. Electrophoresis assisted time-of-flow mass spectrometry using hollow nanomechanical resonators. *Sci. Rep.* **2017**, *7*, 3535.

(41) Ko, J.; Lee, D.; Lee, B. J.; Kang, T.; Kauh, S.; Lee, J. Aspiration and MASS Measurement of Microparticles and Unicellular Organisms via Micropipette Resonators, 2019 20th International Conference on Solid-State Sensors, Actuators and Microsystems & Eurosensors XXXIII (TRANSDUCERS & EUROSENSORS XXXIII), 23–27 June 2019, 2019; pp 748–751.

(42) Lee, J.; Khan, F.; Thundat, T.; Lee, J. Dual Channel Microfluidic Resonators for Simultaneous Measurements of Liquid Analytes, 2019 20th International Conference on Solid-State Sensors, Actuators and Microsystems & Eurosensors XXXIII (TRANSDUCERS & EUROSENSORS XXXIII), 23–27 June 2019, 2019; pp 2088–2090.

(43) Martín-Pérez, A.; Ramos, D.; Tamayo, J.; Calleja, M. Real-Time Particle Spectrometry in Liquid Environment Using Microfluidic-Nanomechanical Resonators. 2019 20th International Conference on Solid-State Sensors, Actuators and Microsystems & Eurosensors XXXIII (TRANSDUCERS & EUROSENSORS XXXIII), 23–27 June 2019, 2019; pp 2146–2149.

(44) Martín-Pérez, A.; Ramos, D.; Tamayo, J.; Calleja, M. Coherent Optical Transduction of Suspended Microcapillary Resonators for Multi-Parameter Sensing Applications. *Sensors* **2019**, *19*, 5069–5078.

(45) Ramos, D.; Tamayo, J.; Mertens, J.; Calleja, M.; Zaballos, A. Origin of the response of nanomechanical resonators to bacteria adsorption. *J. Appl. Phys.* **2006**, *100*, 106105–106108.

(46) Tamayo, J.; Ramos, D.; Mertens, J.; Calleja, M. Effect of the adsorbate stiffness on the resonance response of microcantilever sensors. *Appl. Phys. Lett.* **2006**, *89*, 224104–224107.

(47) Olcum, S.; Cermak, N.; Wasserman, S. C.; Manalis, S. R. High-speed multiple-mode mass-sensing resolves dynamic nanoscale mass distributions. *Nat. Commun.* **2015**, *6*, 7070.

(48) Geltmeier, A.; Rinner, B.; Bade, D.; Meditz, K.; Witt, R.; Bicker, U.; Bludszweit-Philipp, C.; Maier, P. Characterization of Dynamic

Behaviour of MCF7 and MCF10A Cells in Ultrasonic Field Using Modal and Harmonic Analyses. *PLoS One* **2015**, *10*, e0134999–e0135018.

(49) Damania, D.; Subramanian, H.; Backman, V.; Anderson, E. C.; Wong, M. H.; McCarty, O. J. T.; Phillips, K. G. Network signatures of nuclear and cytoplasmic density alterations in a model of pre and postmetastatic colorectal cancer. *J. Biomed. Opt.* **2014**, *19*, 016016.

(50) Liang, X. J.; Liu, A. Q.; Lim, C. S.; Ayi, T. C.; Yap, P. H. Determining refractive index of single living cell using an integrated microchip. *Sens. Actuators, A* **2007**, *133*, 349–354.

(51) Kimmerling, R. J.; Prakadan, S. M.; Gupta, A. J.; Calistri, N. L.; Stevens, M. M.; Olcum, S.; Cermak, N.; Drake, R. S.; Pelton, K.; De Smet, F.; Ligon, K. L.; Shalek, A. K.; Manalis, S. R. Linking single-cell measurements of mass, growth rate, and gene expression. *Genome Biol.* **2018**, *19*, 207.

(52) Wu, M.; Singh, A. K. Single-cell protein analysis. *Curr. Opin. Biotechnol.* **2012**, *23*, 83–88.

(53) Sachs, K.; Perez, O.; Pe'er, D.; Lauffenburger, D. A.; Nolan, G. P. Causal Protein-Signaling Networks Derived from Multiparameter Single-Cell Data. *Science* **2005**, *308*, 523–529.